

# Observation of quasi-two-dimensional Dirac fermions in ZrTe<sub>5</sub>

Xiang Yuan<sup>1,2†</sup>, Cheng Zhang<sup>1,2†</sup>, Yanwen Liu<sup>1,2</sup>, Chaoyu Song<sup>1,2</sup>,  
Shoudong Shen<sup>1,2</sup>, Xing Sui<sup>1,2</sup>, Jie Xu<sup>1,2</sup>, Haochi Yu<sup>1,2</sup>, Zhenghua An<sup>1,2</sup>, Jun Zhao<sup>1,2</sup>,  
Hugen Yan<sup>1,2\*</sup>, Faxian Xiu<sup>1,2\*</sup>

<sup>1</sup> State Key Laboratory of Surface Physics and Department of Physics, Fudan University,  
Shanghai 200433, China

<sup>2</sup> Collaborative Innovation Center of Advanced Microstructures, Fudan University,  
Shanghai 200433, China

<sup>†</sup> These authors contributed equally to this work.

\* Correspondence and requests for materials should be addressed to F. X. (E-mail: [faxian@fudan.edu.cn](mailto:faxian@fudan.edu.cn)), and H. Y. (E-mail: [hgyan@fudan.edu.cn](mailto:hgyan@fudan.edu.cn)).

## Abstract

Since the discovery of graphene<sup>1, 2</sup>, layered materials have attracted extensive interests owing to their unique electronic<sup>3</sup> and optical<sup>4</sup> characteristics. Among them, Dirac semimetal, one of the most appealing categories, has been a long-sought objective in layered systems beyond graphene.<sup>5, 6</sup> Recently, layered pentatelluride ZrTe<sub>5</sub> was found to host signatures of Dirac semimetal.<sup>7, 8</sup> However, the low Fermi level in ZrTe<sub>5</sub> strongly hinders a comprehensive understanding of the whole picture of electronic states through photoemission measurements, especially in the conduction band.<sup>7, 9</sup> Here, we report the observation of Dirac fermions in ZrTe<sub>5</sub> through magneto-optics and magneto-transport. By applying magnetic field, we observe a  $\sqrt{B}$ -dependence of inter-Landau-level resonance and Shubnikov-de Haas (SdH) oscillations with non-trivial Berry phase, both of which are hallmarks of Dirac fermions. The angular-dependent SdH oscillations show a clear quasi-two-dimensional feature with highly anisotropic effective mass and Fermi velocity, in stark contrast to the 3D Dirac semimetal such as Cd<sub>3</sub>As<sub>2</sub>. With the confined interlayer dispersion and reducible dimensionality, our work establishes ZrTe<sub>5</sub> as an ideal platform for exploring exotic physical phenomena of Dirac fermions.

Layered materials, formed by stacking strongly bonded layers with weak interlayer coupling, have drawn immense attention in fundamental studies and device applications owing to their tunability in band structures and Fermi energy.<sup>3, 4, 10, 11, 12</sup> Unlike other layered materials such as MoS<sub>2</sub> and BN, graphene stands out as an appealing candidate as it is featured by a linear energy dispersion and low-energy relativistic quasi-particles.<sup>13, 14</sup> Many exotic phenomena, such as half-integer quantum Hall effect<sup>1, 2</sup> and Klein tunneling<sup>15</sup>, have been realized in graphene. Along this line, extensive efforts were also devoted to explore new Dirac semimetal states in other layered systems beyond graphene.<sup>5, 6</sup>

Pentatelluride ZrTe<sub>5</sub> with layered orthorhombic structure has been widely studied since 1980s for the resistivity anomaly<sup>16, 17</sup> and large thermo-power<sup>18, 19</sup>. For a long time, ZrTe<sub>5</sub> was considered to be a semimetal or degenerated semiconductor with a parabolic energy dispersion.<sup>9, 20</sup> However, a recent study<sup>7</sup> revealed a linear dispersion in ZrTe<sub>5</sub> bulk states along with a chiral magnetic effect, hosting the signatures of Dirac semimetal. Nevertheless, owing to the relatively low Fermi level in ZrTe<sub>5</sub>, a complete understanding of the band structure, especially the conduction band, remains elusive, which makes it challenging to confirm the existence of Dirac fermions. Meanwhile, the layered structure of ZrTe<sub>5</sub> gives rise to a weak interlayer coupling, which should release the confinement on the interlayer dispersion of Dirac fermions as in the case of cuprates.<sup>21</sup> The interplay between Dirac fermions and the interlayer confinement may result in intriguing physical properties yet to be explored.

Here we report the observation of massless Dirac fermions in layered ZrTe<sub>5</sub> based on two independent experiments: magneto-optics and magneto-transport. External magnetic field leads to Landau quantization of Bloch electrons, which enables us to probe the band structure and carrier dynamics in ZrTe<sub>5</sub>. A  $\sqrt{B}$ -dependence of inter-Landau-level resonance is observed, indicating a linear band dispersion. Owing to the high electron mobility and low Fermi level, we are able to detect the Shubnikov-de Haas (SdH) oscillations close to quantum limit, from which a non-trivial Berry phase is obtained. Both of them are well-established signatures for ultra-relativistic quasi-particles in crystals. Furthermore, the angular-dependent magneto-transport reveals a quasi-two-dimensional Fermi surface. The extracted transport parameters infer a strong anisotropy with a large enhancement of effective mass  $m^*$  and a reduction of Fermi velocity  $v_F$  along the b-axis (the layer-stacking direction).

Under external magnetic field  $B$ , the charged particles can occupy discrete orbits and form Landau levels. In classical system described by Schrodinger equation, by ignoring the dispersion along parallel direction, the energy of each Landau level can be strictly derived as  $E_n = (n + 1/2)\hbar\omega_c, n = 0, 1, 2, \dots$  where  $\omega_c = eB/m^*$ ,  $n$ ,  $\hbar$  and  $e$  denote the cyclotron angular frequency, Landau level index, reduced Plank's constant and elementary charge, respectively. Since  $E_n$  increases linearly with  $B$ , the magneto-optics measurement is usually applied to obtain the effective mass  $m^*$  of these classical quasi-particles. However, in Dirac materials, where the electron is described by Dirac equation, if ignoring the parallel dispersion, the energy of the relativistic quasi-

particle can be derived as

$$E_n = \text{sgn}(n)\sqrt{2v_F^2 eB\hbar |n|}, n = 0, 1, 2, \dots \quad (1)$$

Here  $E_n$  follows a square root relation with magnetic field as depicted in Fig. 1a. Fermi velocity determines the evolution of Landau level energy in Dirac systems with magnetic field.

Landau level transitions give resonance peaks in the reflection spectra. To confirm the validity of Equation (1) in ZrTe<sub>5</sub>, we measured the reflection spectra of bulk ZrTe<sub>5</sub> crystals under various magnetic fields at liquid helium temperature. Single crystal ZrTe<sub>5</sub> used in this study was grown by iodine vapor transport method. The as-grown crystals crystallized in the orthorhombic layered structured with space group  $D_{2h}^{17}$ .<sup>16</sup> The prismatic chains of ZrTe<sub>3</sub> run along a-axis and are linked by the zigzag chains of Te along c-axis. These two dimensional layers then stack along b-axis forming the bulk crystal. In order to avoid oxidation and contamination, the samples were freshly cleaved prior to experiments. During the magneto-infrared measurements, the magnetic field is parallel to the b-axis (stacking axis) of the samples. The measured reflection spectra are normalized by the spectrum at zero magnetic field. The detailed experimental setup for the magneto-infrared measurements is provided in the supplementary Fig. S1. Several reflection peaks can be well resolved in the normalized reflection spectra measured under different magnetic fields (Fig. 1b inset). The blocked grey area is originated from 60 Hz harmonics. Since these reflection maxima systematically shift towards higher energy with increasing magnetic field, we conclude the resonance coming from inter-

Landau-level transitions, as determined by electric-dipole-selection rules.<sup>22</sup> The incident photons excite the electrons from the occupied valance band to the unoccupied conduction band (Fig. 1a) following  $\Delta n = n \pm 1$ . Thus, the resonance energy of inter-Landau-level transitions is given by

$$E_{\text{resonance}} = E_n + E_{n+1} = 2v_F \sqrt{eB\hbar} (\sqrt{n} + \sqrt{n+1}), n = 0, 1, 2, \dots \quad (2)$$

The energy ratio between the second (right) and first (left) resonance peaks (Fig. 1b inset) is 1.3, almost the same value as  $(\sqrt{2} + \sqrt{3}) : (\sqrt{1} + \sqrt{2})$ . So the first peak is assigned to be the transition from  $L_{-1}$  to  $L_2$  or from  $L_{-2}$  to  $L_1$  (orange arrows in Fig. 1a), where  $L_n$  represents the  $n^{\text{th}}$  Landau level. Peaks at higher energy should correspond to higher Landau level index. Keeping this in mind, we plot the peak positions with  $\sqrt{n} + \sqrt{n+1}$ . As shown in Fig. 1b, for different magnetic fields, the data points are well aligned to a straight line with y-axis offset close to zero, proving the validity of Equation (1) and (2) and the Landau index assignment. These phenomena show a striking difference from classical systems, in which Landau levels are equally spaced. The assignment of Landau index quantitatively leads to a Fermi velocity of  $v_F = 2 \times 10^5$  m/s, which corresponds to the average slope of the band dispersion in  $k_a$ - $k_c$  plane.

Another key feature of massless Dirac fermions in magneto-infrared spectra,<sup>14, 22, 23</sup> as expressed by Equation (1), is the  $\sqrt{B}$ -dependence of transition energy for the fixed Landau index. In order to analyze the evolution of the peak position with the magnetic field (Fig. 2 inset), we plotted the peak position of normalized reflection spectrum against  $\sqrt{B}$  (Fig. 2). It's evident that the peak position of one Landau level transition

under different fields forms a straight line, indicating a  $\sqrt{B}$  -dependence of resonance energy which is different from the  $B$ -dependence for a classical system. The straight lines in Fig. 2 are the linear fit to the peak positions which point to the origin of the coordinates, consistent with Equation (2). The slopes of the lines derive the same value of Fermi velocity as determined in Fig. 1b. The Landau index can be also obtained from comparing the slopes of different sets of transitions. The most prominent peaks in Fig. 1b inset are determined to be  $L_{-2}$  to  $L_1$  ( $L_{-1}$  to  $L_2$ ). We note that the transition for lower index ( $L_0$  to  $L_1$ ) is not observable due to the strong phonon absorption of ZrTe<sub>5</sub> when the excitation energy is lower than 200 cm<sup>-1</sup> (Fig. S2). Both  $\sqrt{n}$  and  $\sqrt{B}$  dependence in the magneto-infrared study provides a consolidate evidence for the existence of Dirac fermions in ZrTe<sub>5</sub>.

To acquire in-depth understanding of the Fermi surface, we carried out magneto-transport measurements with rotatable field direction. As schematically illustrated in Fig. 3a, conventional six-terminal devices were prepared with a constant current applied along the a-axis of the single crystal. Similar to the previous studies,<sup>16, 17, 24</sup> we observed several unique features of ZrTe<sub>5</sub>, such as “resistivity anomaly” and Hall sign reversal at 140K (refer to Fig. S4). As determined from Hall effect (Fig. S5), ZrTe<sub>5</sub> has an  $n$ -type conductivity at low temperatures. Fig. 3b exhibits the magneto-resistivity (MR) of ZrTe<sub>5</sub> with the magnetic field tilting from b-axis to a-axis. It is evident that the rotation of the magnetic field from perpendicular to parallel to the a-c plane causes a sharp decrease of MR. Apart from the giant anisotropic MR, we observed clear SdH

oscillations as a result of Landau quantization. The oscillations can be well resolved from MR (Fig. 3b) even with the magnetic field lower than 1T, which indicates a high carrier mobility in ZrTe<sub>5</sub>, consistent with the Hall effect measurements (Fig. S5&6). The amplitude of the oscillations decreases with the increase of temperature but the oscillatory frequency remains the same (Fig. 3c).

Generally, under a perpendicular magnetic field  $B$ , closed cyclotron orbits follow the Lifshitz-Onsager quantization rule,

$$S_F \frac{\hbar}{eB} = 2\pi(n + \gamma) = 2\pi\left(n + \frac{1}{2} - \frac{\phi_B}{2\pi}\right) \quad (3)$$

where  $S_F$  is the cross-sectional area of Fermi surface related to the Landau index  $n$ , and  $\phi_B$  is a geometrical phase known as Berry phase. In a Dirac system, the  $k$ -space cyclotron orbits enclose a Dirac point so that there exists a “zero mode” that does not shift with  $B$ , resulting in a non-trivial Berry phase  $\phi_B = \pi$ .<sup>13, 14, 25</sup> And  $\gamma$ , defined as  $\gamma \equiv 1/2 - \phi_B/2\pi$ , can be quantitatively determined by analyzing the intercept of Landau fan diagram from the SdH oscillations. The non-trivial Berry phase generally serves as a key evidence for Dirac fermions and has been observed in several well-known Dirac materials such as graphene<sup>2, 13</sup>, topological insulator<sup>26, 27</sup>, and Cd<sub>3</sub>As<sub>2</sub><sup>28, 29</sup>. Here we present the Landau fan diagram in Fig. 3d, where  $n$  and  $1/B_n$  are extracted from the peak positions in the MR curves. We only use the data below 3T in this plot since the SdH oscillations are overwhelmed by a huge shoulder-like MR background at higher field. By performing a linear fit, the intercept on y-axis is determined to be  $0 \pm 0.04$ , corresponding to the non-trivial Berry phase. In addition, the slope of the

Landau fan diagram gives the frequency of SdH oscillation,  $F=5.3$  T, corresponding to an extremely small Fermi surface of  $S_F = 8 \times 10^{-5} \text{ \AA}^{-2}$ .

Important transport parameters can be obtained from the SdH oscillation analysis.<sup>30</sup> The temperature dependence of oscillation amplitude  $\Delta\rho$  is shown in Fig. 3e, which is described by the formula  $\Delta\rho(T) = \Delta\rho(0)\lambda(T) / \sinh(\lambda(T))$ . The thermal factor  $\lambda(T)$  is given by  $\lambda(T) = 2\pi^2 k_B T m^* / \hbar e B$ , where  $k_B$  is Boltzmann's constant and  $m^*$  is the effective mass. By performing the best fit to the equation, a small effective mass of  $m^* = 0.03m_e$  is derived with  $m_e$  being the electron mass. Thus  $v_F = 5 \times 10^5$  m/s can be calculated based on  $\hbar k_F = m^* v_F$ . Note that the  $v_F$  values extracted from the magneto-optics, low-temperature transport and angle-resolved photoemission experiments are on the same order but with finite variations, probably due to the electron-phonon interaction<sup>31,32</sup> or extrinsic effect<sup>33</sup>. We can also estimate the transport life time  $\tau$  by considering Dingle factor  $e^{-D}$ , where  $D = 2\pi^2 E_F / \tau e B v_F^2$ . Note that  $\Delta R / R_0$  is proportional to  $[\lambda(T) / \sinh(\lambda(T))] e^{-D}$ , so the lifetime can be inferred from the slope in the logarithmic plot (Fig. 3f). By using  $m^* = 0.03m_e$ , the life time of ZrTe<sub>5</sub> can be estimated to be  $\tau = 1 \times 10^{-12}$  s. A relatively high quantum mobility can be acquired by  $\mu = e\tau / m^* = 7 \times 10^4$  cm<sup>2</sup>/Vs.

To investigate the overall Fermi surface geometry in ZrTe<sub>5</sub>, we performed angular-dependent magneto-transport measurements. As shown in Fig. 4a, MR with different field directions is distinguished by colors. A noticeable feature is that all curves overlap

with each other when plotted against  $B \cos \theta$ . At  $\theta = 90^\circ$ , the longitudinal MR is almost fully suppressed. The close relationship between the MR ratio and out-of-plane magnetic field indicates a 2D-like behavior of the detected orbit. The shape of overall Fermi sphere can be mapped by the angular-dependent SdH oscillations. Fig. 4b and Fig. 4c demonstrate the extracted SdH oscillations while the magnetic field was tilted from b-axis to a-axis and from b-axis to c-axis, respectively. Similar to the MR background which are overlapped in scale of  $B \cos \theta$ , the peaks and valleys of the subtracted oscillations are aligned when plotted with respect to  $B \cos \theta$ , in stark contrast with those isotropic three-dimensional systems<sup>34</sup>. Fig. 4d shows a Fast-Fourier-Transfer (FFT) analysis of the SdH oscillations. The single peak feature in the FFT spectra corresponds to a single-band transport. For an ideal 2D system, the oscillation frequency  $F$  increases linearly with  $1 / \cos \theta$  and becomes infinitely at  $\theta = 90^\circ$  due to the infinite cross-section of Fermi surface. In Fig. 4e and Fig. 4f, we plotted the ideal 2D curve following  $1 / \cos \theta$  rule. Here, the experimental oscillation frequency  $F$  increases with  $1 / \cos \theta$  and shows a saturation behavior with a small deviations when approaching  $90^\circ$ . The saturation of the frequency suggests a large but not infinite Fermi surface on b-c plane. Combining the trend of the MR background and the SdH oscillations with various field directions, we can conclude that the Fermi surface in ZrTe<sub>5</sub> is highly anisotropic and shows long-rod-like shape in the reciprocal space thus possessing a quasi-2D behavior in real space.

Analysis of SdH oscillations at orthogonal three axes was further conducted to

investigate the detailed band dispersion characteristics along different directions. Fig.5a is the oscillation amplitude plotted as a function of temperature. The best fit to those data yields the effective mass for each plane ( $k_b$ - $k_c$ ,  $k_a$ - $k_c$ , and  $k_a$ - $k_b$ ). The Fermi velocity of each plane can be also calculated as discussed above. The a-c plane shows a much smaller  $m^*$  and a larger  $v_F$  compared with the other two (Fig. 5b). As mentioned earlier, the parameters derived from the Landau quantization through transport and magneto-optics are an average value over the closed cyclotron orbit. With the low Fermi level in ZrTe<sub>5</sub>, the boundary of Brillouin Zone should not have a large impact on the shape of Fermi surface. Thus, we can safely take the Fermi surface as an ellipsoid and the Fermi velocity (effective mass) of each plane is described as, for example,  $v_{a-c} = \sqrt{v_a v_c}$ . Here,  $v_a$  and  $v_c$  are the corresponding Fermi velocity along  $k_a$  and  $k_c$ , respectively. The transport parameters along different axes are extracted as shown in Fig. 5c. The  $m^*$  (red bar) shows a strong anisotropy with a large enhancement along b-axis. It is natural to observe the relatively small effective mass of  $0.02m_e$  &  $0.05m_e$  in respectively a-axis and c-axis, consistent with the observation of massless Dirac fermion in a-c plane from our magneto-optics experiments. However, the large effective mass of  $1.3m_e$  along b-axis is unexpected for the conventional three-dimensional Dirac materials. Note that the crystal is stacked by the layers on a-c plane along b-axis. The large effective mass may be denoted by the quadratic band dispersion<sup>35</sup> due to the weak interlayer coupling as illustrated in Fig. 5d. The much lower Fermi velocity (Fig. 5c) and quantum mobility (Fig. S9) along b-axis also support our assumption. On the other hand, there is a relatively large difference both in  $m^*$  and  $v_F$  between a-axis and c-axis,

revealing an anisotropy in the in-plane dispersion of Dirac Cone.

The ab initio calculations have predicted the interlayer binding energy for ZrTe<sub>5</sub> as 12.5 meV/Å, a comparable value to graphite (9.3 meV/Å), suggesting the weak interlayer coupling.<sup>36</sup> Using the conventional scotch tape method, we have also successfully exfoliated ZrTe<sub>5</sub> into 2D thin flakes (Fig. S10). We found that, upon the exfoliation, not only the inter-plane Van der Waals force is easy to overcome, but the in-plane Te zigzag chains are also readily broken, thus developing a quasi-one-dimensional structure (Fig. S11). The relatively weak bond along c-axis may be the reason for the increase of  $m^*$  and the decrease of  $v_F$ , similar to the case of the b-axis.

Since both the magneto-optics and magneto-transport measurements were performed near liquid helium temperature, our conclusion of massless Dirac fermion is valid in the low temperature range. But the resistivity and Hall measurements near 140 K (Fig. S4) reveal a metal-semiconductor transition (anomaly peak) along with Hall sign reversal (Fig. S4), indicating a multi-carrier transport and a complex band structure evolving with temperature. However, for higher temperatures, when thermal energy is larger than the energy level separation ( $k_B T > \hbar \omega_c$ ), Landau quantization is no longer accessible, which calls for further experimental efforts to elucidate the detailed band structure. Judging from the Landau fan diagram (Fig. 3d), the first Landau level can be accessed within 6T in magneto-transport. The low Fermi level is also indicated by the magneto-optics measurements since the transition of low index Landau level is

available at comparably low fields. Considering the low Fermi level, the thin flakes of  $\text{ZrTe}_5$  may be also suitable for static electrical gating, which may add another new degree of freedom to help understanding the anomalous transport behavior along different axes or at high temperatures. Meanwhile, it will be of substantial interests to see whether it will sustain the Dirac semimetal states as in bulk form or transfer into a quantum spin Hall insulator as theory predicted when approaching the 2D limit. Further experiments in the nanoscale samples of  $\text{ZrTe}_5$  are currently being pursued.

In conclusion, we confirm the Dirac semimetal state in bulk  $\text{ZrTe}_5$  by magneto-optics and SdH oscillations. Angular-dependent quantum oscillations further reveal a quasi-2D nature of the Dirac fermions. The unusual interlayer dispersion characteristics, low Fermi level, and van der Waals structure demonstrate  $\text{ZrTe}_5$  as an intriguing system for both the fundamental studies and device applications.

## **Method**

### **Single Crystal synthesis.**

High-quality  $\text{ZrTe}_5$  single crystals were synthesized by iodine vapor transport method in a two-zone tube furnace. Stoichiometric amounts of high-purity Zr and Te elements were placed in a quartz tube and sealed under vacuum. The growth rate along a-axis is much faster than those in b-axis and c-axis, yielding needle-like samples. The chemical ratio is found to be 1:5 for Zr/Te, determined by energy dispersive x-ray analysis in scanning electron microscopy.

**Magneto-optics measurements.**

ZrTe<sub>5</sub> was freshly cleaved, subject to an applied magnetic field parallel to the stacking axis (Faraday geometry) at liquid helium temperature. An infrared light from a broadband light source is modulated by interferometer and vibration mirrors in the Fourier-transfer infrared spectrometer (FTIR). The light was guided through a light pipe and focused on the sample with millimeter spot by a parabolic cone (Fig. S1). A bolometer was used to measure the intensity of reflection light simultaneously with FTIR.

**Magneto-transport measurements.**

Freshly cleaved ZrTe<sub>5</sub> was measured using standard six-terminal Hall-bar geometry in a physical property measurement system. Stanford Research 830 Lock-in amplifiers were used to measure the electrical signals with magnetic field up to 9T that applied for various orientations of the applied magnetic field.

**Sample exfoliation.**

ZrTe<sub>5</sub> was firstly exfoliated on scotch tape and then transferred onto 300nm/300μm SiO<sub>2</sub>/Si substrate. The flakes with different thickness can be identified by different colors. In order to enhance the productivity of one dimensional structure and avoid contamination, PDMS (polydimethylsiloxane) was used to transfer the exfoliated samples.

## Reference

1. Novoselov K, Geim AK, Morozov S, Jiang D, Katsnelson M, Grigorieva I, *et al.* Two-dimensional gas of massless Dirac fermions in graphene. *Nature* 2005, **438**(7065): 197-200.
2. Zhang Y, Tan YW, Stormer HL, Kim P. Experimental observation of the quantum Hall effect and Berry's phase in graphene. *Nature* 2005, **438**(7065): 201-204.
3. Fiori G, Bonaccorso F, Iannaccone G, Palacios T, Neumaier D, Seabaugh A, *et al.* Electronics based on two-dimensional materials. *Nature nanotechnology* 2014, **9**(10): 768-779.
4. Wang QH, Kalantar-Zadeh K, Kis A, Coleman JN, Strano MS. Electronics and optoelectronics of two-dimensional transition metal dichalcogenides. *Nature nanotechnology* 2012, **7**(11): 699-712.
5. Kim J, Baik SS, Ryu SH, Sohn Y, Park S, Park B-G, *et al.* Observation of tunable band gap and anisotropic Dirac semimetal state in black phosphorus. *Science* 2015, **349**(6249): 723-726.
6. Qian X, Liu J, Fu L, Li J. Quantum spin Hall effect in two-dimensional transition metal dichalcogenides. *Science* 2014, **346**(6215): 1344-1347.
7. Li Q, Kharzeev DE, Zhang C, Huang Y, Pletikosic I, Fedorov A, *et al.* Observation of the chiral magnetic effect in ZrTe5. *arXiv preprint arXiv:14126543* 2014.
8. Chen RY, Zhang SJ, Schneeloch JA, Zhang C, Li Q, Gu GD, *et al.* Optical spectroscopy study of the three-dimensional Dirac semimetal ZrTe5. *Physical Review B* 2015, **92**(7): 075107.
9. McIlroy DN, Moore S, Zhang D, Wharton J, Kempton B, Littleton R, *et al.* Observation of a semimetal–semiconductor phase transition in the intermetallic ZrTe5. *Journal of Physics: Condensed Matter* 2004, **16**(30): L359-L365.
10. Xu X, Yao W, Xiao D, Heinz TF. Spin and pseudospins in layered transition metal dichalcogenides. *Nature Physics* 2014, **10**(5): 343-350.
11. Geim AK, Grigorieva IV. Van der Waals heterostructures. *Nature* 2013, **499**(7459): 419-425.
12. Xu M, Liang T, Shi M, Chen H. Graphene-like two-dimensional materials. *Chemical reviews* 2013, **113**(5): 3766-3798.
13. Neto AC, Guinea F, Peres N, Novoselov KS, Geim AK. The electronic properties of graphene. *Reviews of Modern Physics* 2009, **81**(1): 109.

14. Basov DN, Fogler MM, Lanzara A, Wang F, Zhang Y. Colloquium: Graphene spectroscopy. *Reviews of Modern Physics* 2014, **86**(3): 959-994.
15. Young AF, Kim P. Quantum interference and Klein tunnelling in graphene heterojunctions. *Nature Physics* 2009, **5**(3): 222-226.
16. Skelton E, Wieting T, Wolf S, Fuller W, Gubser DU, Francavilla T, *et al.* Giant resistivity and X-ray diffraction anomalies in low-dimensional ZrTe<sub>5</sub> and HfTe<sub>5</sub>. *Solid State Communications* 1982, **42**(1): 1-3.
17. Fuller W, Wolf S, Wieting T, LaCoe R, Chaikin P, Huang C. Pressure effects in HfTe<sub>5</sub> and ZrTe<sub>5</sub>. *Le Journal de Physique Colloques* 1983, **44**(C3): C3-1709-C1703-1712.
18. Jones T, Fuller W, Wieting T, Levy F. Thermoelectric power of HfTe<sub>5</sub> and ZrTe<sub>5</sub>. *Solid State Communications* 1982, **42**(11): 793-798.
19. Littleton IV R, Tritt TM, Kolis J, Ketchum D. Transition-metal pentatellurides as potential low-temperature thermoelectric refrigeration materials. *Physical Review B* 1999, **60**(19): 13453.
20. Whangbo M-H, DiSalvo F, Fleming R. Electronic structure of ZrTe<sub>5</sub>. *Physical Review B* 1982, **26**(2): 687.
21. Vafeek O, Vishwanath A. Dirac Fermions in Solids: From High-Tc Cuprates and Graphene to Topological Insulators and Weyl Semimetals. *Annual Review of Condensed Matter Physics* 2014, **5**(1): 83-112.
22. Orlita M, Basko DM, Zholudev MS, Teppe F, Knap W, Gavrilenko VI, *et al.* Observation of three-dimensional massless Kane fermions in a zinc-blende crystal. *Nature Physics* 2014, **10**(3): 233-238.
23. Jiang Z, Henriksen E, Tung L, Wang Y-J, Schwartz M, Han M, *et al.* Infrared spectroscopy of Landau levels of graphene. *Physical review letters* 2007, **98**(19): 197403.
24. Tritt TM, Lowhorn ND, Littleton IV R, Pope A, Feger C, Kolis J. Large enhancement of the resistive anomaly in the pentatelluride materials HfTe<sub>5</sub> and ZrTe<sub>5</sub> with applied magnetic field. *Physical Review B* 1999, **60**(11): 7816.
25. Hasan MZ, Kane CL. Colloquium: Topological insulators. *Reviews of Modern Physics* 2010, **82**(4): 3045-3067.
26. Analytis JG, McDonald RD, Riggs SC, Chu J-H, Boebinger G, Fisher IR. Two-dimensional surface state in the quantum limit of a topological insulator. *Nature Physics* 2010, **6**(12): 960-964.

27. Zhang C, Yuan X, Wang K, Chen ZG, Cao B, Wang W, *et al.* Observations of a Metal–Insulator Transition and Strong Surface States in Bi<sub>2–x</sub>Sb<sub>x</sub>Se<sub>3</sub> Thin Films. *Advanced materials* 2014, **26**(41): 7110-7115.
28. He LP, Hong XC, Dong JK, Pan J, Zhang Z, Zhang J, *et al.* Quantum Transport Evidence for the Three-Dimensional Dirac Semimetal Phase in Cd<sub>3</sub>As<sub>2</sub>. *Physical Review Letters* 2014, **113**(24): 246402.
29. Cao J, Liang S, Zhang C, Liu Y, Huang J, Jin Z, *et al.* Landau level splitting in Cd<sub>3</sub>As<sub>2</sub> under high magnetic fields. *Nature communications* 2015, **6**: 7779.
30. Xiu F, He L, Wang Y, Cheng L, Chang LT, Lang M, *et al.* Manipulating surface states in topological insulator nanoribbons. *Nature nanotechnology* 2011, **6**(4): 216-221.
31. Park C-H, Giustino F, Cohen ML, Louie SG. Velocity Renormalization and Carrier Lifetime in Graphene from the Electron-Phonon Interaction. *Physical Review Letters* 2007, **99**(8).
32. Siegel DA, Park C-H, Hwang C, Deslippe J, Fedorov AV, Louie SG, *et al.* Many-body interactions in quasi-freestanding graphene. *Proceedings of the National Academy of Sciences* 2011, **108**(28): 11365-11369.
33. Wolos A, Szyszko S, Drabinska A, Kaminska M, Strzelecka SG, Hruban A, *et al.* Landau-Level Spectroscopy of Relativistic Fermions with Low Fermi Velocity in the Bi<sub>2</sub>Te<sub>3</sub> Three-Dimensional Topological Insulator. *Physical Review Letters* 2012, **109**(24).
34. Liang T, Gibson Q, Ali MN, Liu M, Cava RJ, Ong NP. Ultrahigh mobility and giant magnetoresistance in the Dirac semimetal Cd<sub>3</sub>As<sub>2</sub>. *Nature materials* 2014, **14**(3): 280-284.
35. Park J, Lee G, Wolff-Fabris F, Koh Y, Eom M, Kim Y, *et al.* Anisotropic Dirac fermions in a Bi square net of SrMnBi<sub>2</sub>. *Physical review letters* 2011, **107**(12): 126402.
36. Weng H, Dai X, Fang Z. Transition-Metal Pentatelluride ZrTe<sub>5</sub> and HfTe<sub>5</sub>: A Paradigm for Large-Gap Quantum Spin Hall Insulators. *Physical Review X* 2014, **4**(1): 011002.

## FIGURES

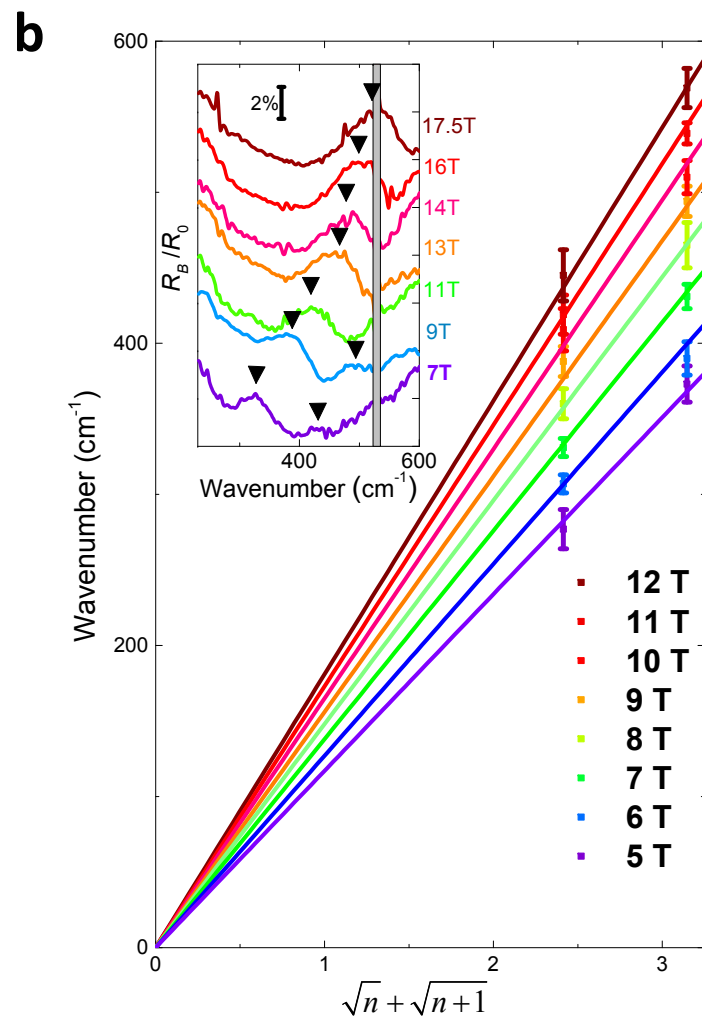
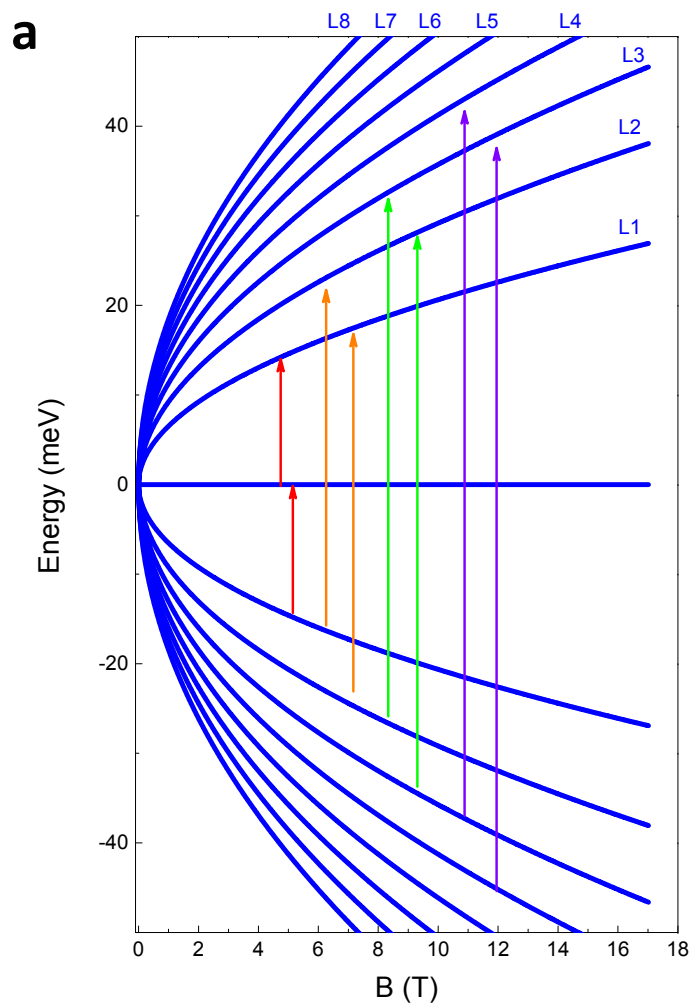
**Figure 1 | Landau-level fan chart and normalized magneto-reflection of ZrTe<sub>5</sub>.** **a**, Landau levels in ZrTe<sub>5</sub> as a function of magnetic field. Arrows show the allowable optical transitions. Different colors denote different resonance energy. **b**, The resonance energy versus  $\sqrt{n} + \sqrt{n+1}$  under different magnetic fields. The straight line is for eye-guide. Inset: Normalized reflection spectra under different magnetic fields. Triangles denote the peak positions.

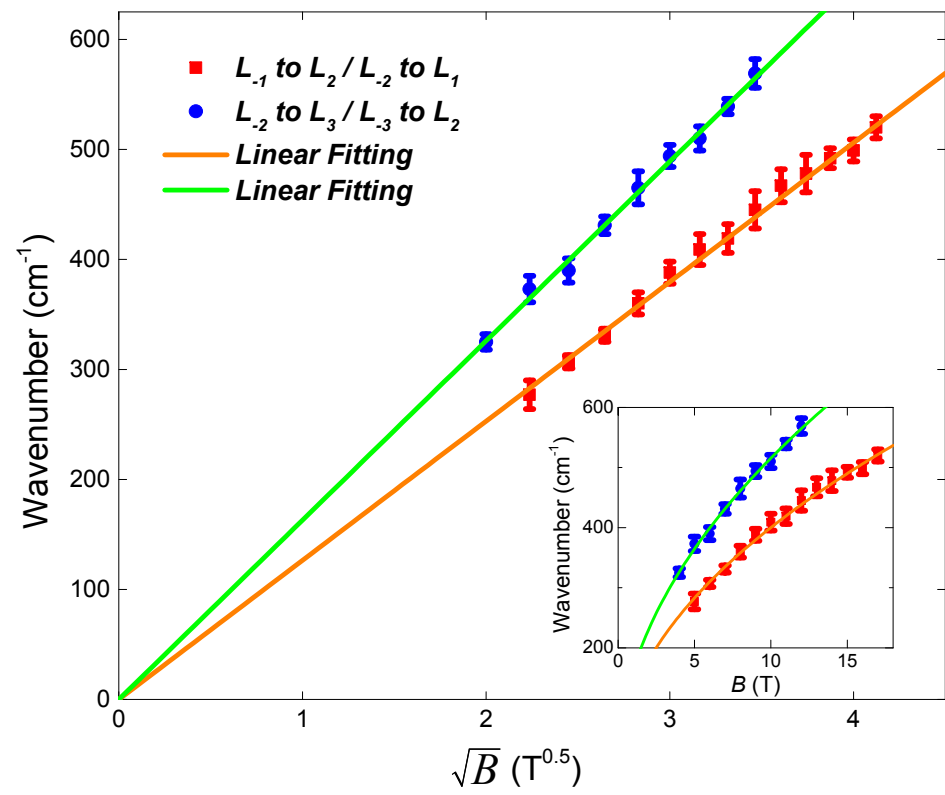
**Figure 2 | Magneto-reflectivity in ZrTe<sub>5</sub>.** Reflectivity maxima frequency plotted with  $\sqrt{B}$ . The observed inter-Landau-level resonance clearly follows a  $\sqrt{B}$  dependence. Inset is the reflectivity maxima frequency versus  $B$ .

**Figure 3 | Magneto-transport measurements in ZrTe<sub>5</sub>.** **a**, Schematic drawing of the transport measurements. A constant current was applied along a-axis. **b**, Angular dependence of MR at 2.5K. The SdH oscillations are observed at different angles. **c**, MR at different temperatures with  $\theta = 0^\circ$ . The oscillations are not observable above 20 K. The inset is an enlarged view of the oscillations. **d**, Landau fan diagram at  $\theta = 0^\circ$ . Non-trivial Berry phase can be clearly determined. **e**, Temperature dependence of the SdH oscillation amplitude at 1.34 T. **f**, Dingle plot for the extraction of the scattering time.

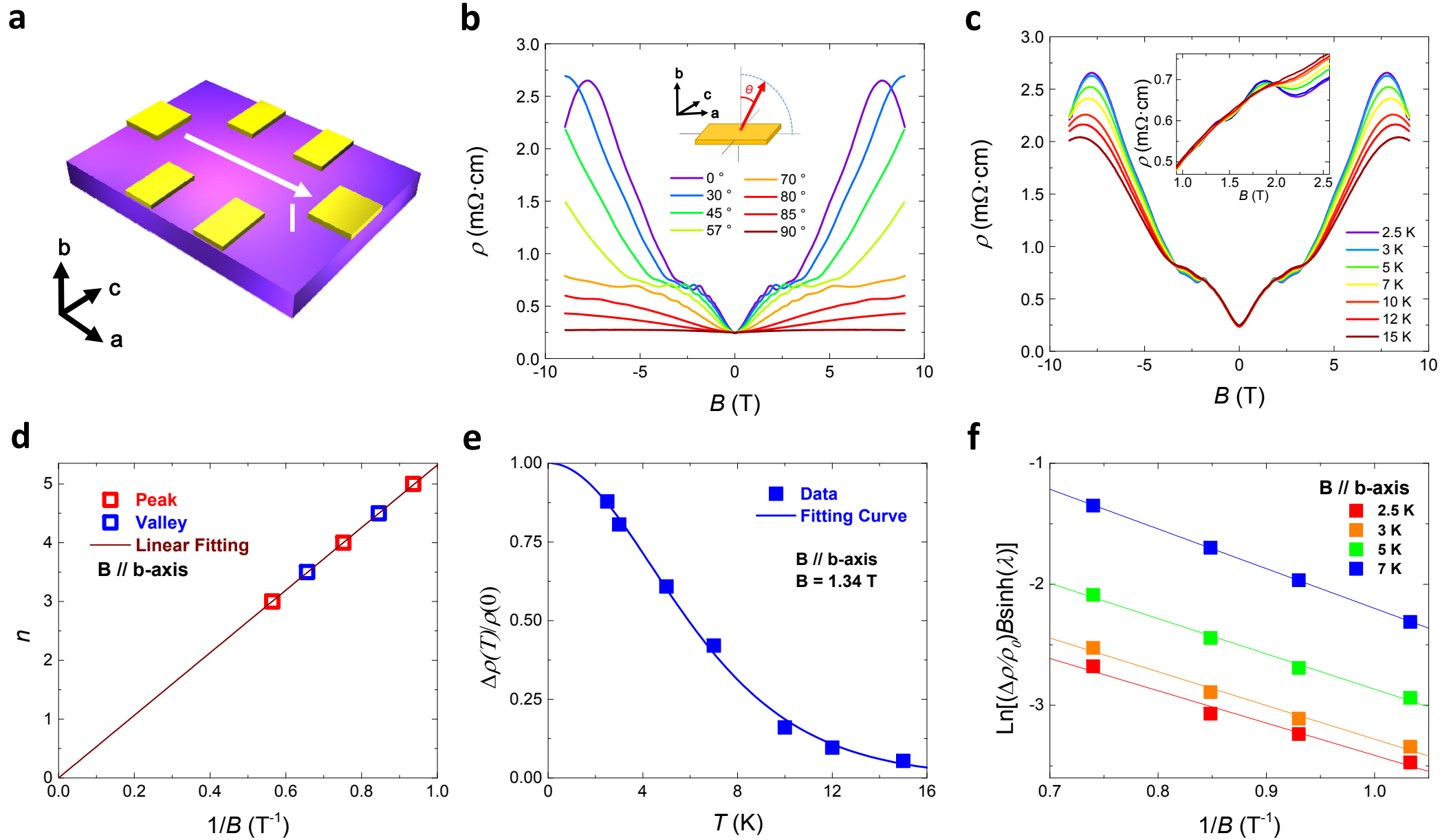
**Figure 4 | Angular-dependent Magneto-transport measurements in ZrTe<sub>5</sub>.** **a**, Resistivity versus magnetic field. Data for different  $\theta$ , denoted by different colors, overlap with each other, indicating a quasi-2D behavior. **b** and **c**, The oscillatory component  $\Delta\rho$  plotted against  $1/B\cos(\theta)$  or  $1/B\cos(\phi)$  for  $B$  rotation along c-axis and a-axis. **d**, FFT spectra for different  $\theta$ . **e** and **f**, Oscillation frequency plotted with angle. The black curve shows an ideal 2D behavior.

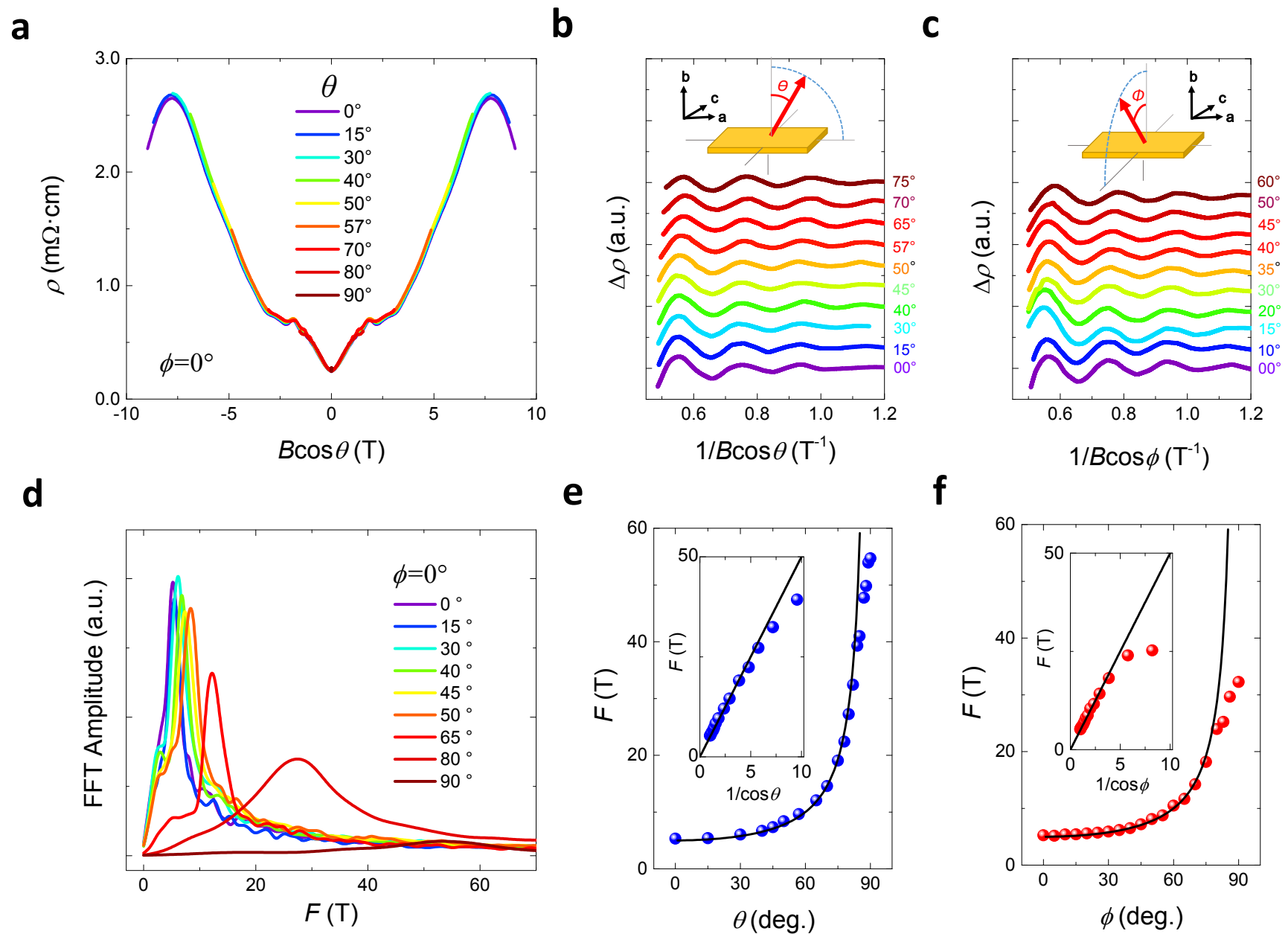
**Figure 5 | Dispersion characteristics along orthogonal axes.** **a**, The temperature dependence of the SdH oscillation amplitude, for magnetic field parallel to c-axis (upper), a-axis (middle) and b-axis (lower). **b**, The effective mass and Fermi velocity retracted from the SdH oscillations in different crystal planes. **c**, The effective mass and Fermi velocity calculated from **b**, based on the ellipsoid model. **d**, A schematic plot for dispersion characteristics along different orientations.





X. Yuan, et al. Figure 2





X. Yuan, et al. Figure 4

